Coordinated Operation of Custom Power Devices for Enhanced Voltage Quality and Harmonic Mitigation in Smart Distribution Networks

[1]Kripa Shanker, Dr. C. V. Raman University, Vaishali, Bihar,

[2]Dr. Dharmendra Kumar Singh, Dr. C. V. Raman University, Vaishali, Bihar

Abstract— This work presents a novel custom power device (CPD) designed for dynamic management of reactive power and enhancement of voltage quality in smart grid (SG) systems under both fundamental and harmonic conditions. The approach utilizes real-time data obtained from smart meters installed at each bus and communicated to the smart grid central controller (SGCC). Based on this information, the CPD simultaneously performs the functions of a static synchronous compensator (STATCOM) and an active power line conditioner (APLC) by optimally compensating fundamental reactive power and harmonic currents at strategically selected buses.

The proposed methodology incorporates two particle swarm optimization (PSO) techniques. The first PSO algorithm is applied under worst-case operating scenarios to identify optimal placement and sizing of CPDs. The second PSO algorithm leverages continuous smart meter data to generate real-time reference signals for both fundamental and harmonic compensation, ensuring effective control of the installed CPDs.

The optimization objectives include minimizing costs related to voltage profile improvement, total harmonic distortion of voltage (THDv), and device sizing, subject to constraints such as maximum CPD capacity and permissible limits of fundamental and harmonic bus voltages. Comprehensive simulations are carried out using MATLAB/Simulink to validate the effectiveness of the proposed approach. The system performance is tested on a distorted 15-bus smart grid with six nonlinear loads, ensuring compliance with IEEE-519 standards.

Keywords: Custom Power Device (CPD), Static Synchronous Compensator (STATCOM), Active Power Line Conditioner (APLC), Reactive Power Compensation, Harmonic Mitigation, Particle Swarm Optimization (PSO).

I. Introduction

Smart grids (SGs) are increasingly being adopted worldwide by both utilities and consumers due to their capability to enhance demand-side management, facilitate real-time monitoring and control of system assets, and improve overall network efficiency and reliability through the deployment of smart meters and

advanced sensing technologies [1–3]. However, the evolution of modern power systems has introduced significant challenges for electric utilities, primarily due to increased network complexity and the growing penetration of nonlinear loads and renewable energy sources. These factors often lead to degraded voltage profiles and increased system losses at both fundamental and harmonic frequencies.

Among various power quality concerns, voltage instability remains one of the most critical issues [4]. For instance, voltage sags account for a substantial proportion—over 80%—of power quality disturbances observed in electrical networks [5]. In extreme scenarios, voltage instability may escalate into voltage collapse, resulting in complete system outages [6]. To mitigate such risks, reactive power compensation techniques are commonly employed prior to reaching critical voltage conditions. Conventional solutions include the installation of shunt capacitor banks (fixed or switched), static var compensators (SVCs) [7], and flexible AC transmission system (FACTS) devices such as static synchronous compensators (STATCOMs) [8], strategically placed within the network.

Switched capacitor banks typically require scheduling based on load demand and distributed generation forecasts. SVCs utilize thyristor-based components, such as thyristor switched capacitors (TSCs) and thyristor-controlled reactors (TCRs), to provide dynamic reactive power support [7]. In comparison, STATCOMs offer advantages including faster dynamic response and reduced physical size due to the absence of bulky passive components. Additionally, unlike SVCs, whose performance depends heavily on system voltage levels, STATCOMs are capable of delivering adequate reactive power even under low-voltage conditions. Nevertheless, these devices are primarily designed for voltage regulation and reactive power control at the fundamental frequency and generally do not address harmonic distortions caused by nonlinear loads.

The injection of harmonic currents leads to voltage distortions and harmonic voltage drops across the network [9]. Such distortions must be maintained within acceptable limits defined by standards such as IEEE-519, which specify permissible levels for total harmonic distortion of current (THDi), voltage (THDv), and individual harmonic components [10]. Conventional mitigation techniques include passive, active, and hybrid filtering solutions. However, these approaches typically focus on limiting harmonics at the point of common coupling (PCC) and may not effectively control voltage distortion throughout the entire network [9]. Installing active power filters (APFs) at every bus with nonlinear loads could address this issue, but it is generally impractical from an economic and operational standpoint [11]. A more viable solution is the deployment of a custom power device (CPD) that integrates the functionalities of FACTS devices and active filters.

As outlined in the draft IEEE P1409 Guideline [12], CPDs are power electronic devices designed to enhance power quality in distribution systems through voltage regulation and/or current control. These devices can be broadly classified into two categories:

1. **Source-oriented CPDs**, which protect the network from load-induced disturbances by providing reactive power compensation and harmonic mitigation. Examples include SVC, D-STATCOM, unified power quality conditioner (UPQC), and active power line conditioner (APLC). Research on APLCs remains limited [13–18], primarily due to the historical lack of real-time system data, a challenge now being addressed through widespread smart meter deployment in SGs.

2. **Load-oriented CPDs**, which safeguard sensitive loads from supply-side disturbances such as voltage sags and swells. Devices in this category include static transfer switches (STS), static series compensators (SSC), static voltage regulators (SVR), as well as D-STATCOMs and dynamic voltage restorers (DVRs) equipped with energy storage systems.

A dynamic voltage restorer (DVR), when connected in series with the distribution network, can effectively regulate and balance three-phase voltages at the load bus while also mitigating voltage harmonics. It operates by injecting appropriate voltage components in series with the supply voltage, thereby compensating for voltage sags and swells. Additionally, it introduces harmonic voltage components to maintain a near-sinusoidal voltage waveform across the load.

Research addressing the simultaneous mitigation of reactive power issues and voltage harmonic distortions remains relatively scarce in the literature [19–24]. In [19], an active power filter (APF) is developed to provide both reactive power support and harmonic compensation for single-phase linear and nonlinear loads. Similarly, [20] introduces a transformer-less universal active filter incorporating both series and shunt configurations for single-phase systems. An improved STATCOM with harmonic suppression capability is presented in [21], while studies in [22–24] focus on unified power quality conditioners (UPQCs) employing combined series and shunt converters to mitigate current distortions and regulate bus voltages.

A review of existing works [8–9, 11–23] indicates that most approaches are limited to specific aspects of power quality improvement. These include reactive power compensation at the point of common coupling (PCC) to stabilize voltage (STATCOM functionality), harmonic current mitigation at PCC to reduce current distortion (APF functionality), or compensation of harmonics at selected buses to improve overall network voltage distortion (APLC functionality). Among these, only [24] considers a network-wide perspective by addressing power quality across the entire system and proposing optimal placement of UPQCs in a radial distribution network. However, this study primarily focuses on reactive power

compensation and determines UPQC allocation based on objectives such as device rating, system power losses, and the number of buses experiencing undervoltage conditions.

The primary objective of this work is to achieve comprehensive reactive power management and harmonic mitigation across the entire smart grid (SG) through optimal placement, sizing, and real-time control of custom power devices (CPDs) capable of simultaneously performing STATCOM and APLC functions. Initially, a particle swarm optimization (PSO) algorithm is employed to determine the optimal locations and ratings of multiple CPDs in a distorted SG environment with nonlinear loads. The optimization aims to minimize overall network voltage total harmonic distortion (THDv) and the total current injected by CPDs, subject to constraints on bus voltage limits, permissible THDv levels, and individual harmonic components.

Subsequently, a second PSO-based framework is developed for real-time operational control of the deployed CPDs using data acquired from smart meters. This enables continuous adaptation to system conditions for effective compensation. The proposed methodology is validated through detailed simulation studies conducted on a 15-bus distorted distribution network [25], incorporating six nonlinear loads.

II. Modeling and Control of the Proposed Custom Power Device (CPD)

This section begins with a brief overview of conventional STATCOM and APLC devices, followed by a comprehensive formulation and modeling of the proposed CPD.

A. Static Synchronous Compensator (STATCOM)

The primary function of a STATCOM is to regulate reactive power flow in the network by injecting or absorbing a controlled amount of reactive power at the point of common coupling (PCC). As a key FACTS device, it enhances power quality in distribution systems by addressing issues such as voltage flicker, sag and swell mitigation, dynamic voltage support, oscillation damping, and reactive power compensation.

A typical STATCOM configuration includes a voltage source converter (VSC), a DC link (comprising a capacitor or energy storage element), a control system, and a coupling transformer that interfaces with the grid. The exchange of active and reactive power at the PCC is governed by the relationship expressed in Equation (1).

$$S = P - jQ = 3\frac{V_s V_C}{X_L}\sin\alpha - j3\left(\frac{V_s V_C}{X_L}\cos\alpha - \frac{V_s^2}{X_L}\right) \quad (1)$$

Here, S, P, and Q represent the apparent, active, and reactive power, respectively. V_s denotes the phase voltage at the connected bus, while V_c corresponds to the fundamental component of the STATCOM output phase voltage. The parameter $X_L = 2\pi fL$ defines the leakage reactance, where f is the system frequency and L is the inductance. The symbol α indicates the phase angle difference between V_s and V_c.

For effective reactive power regulation, the STATCOM operates by injecting either leading or lagging current that is maintained in quadrature with the system voltage. The schematic representation of a STATCOM power circuit is illustrated in Fig. 1.

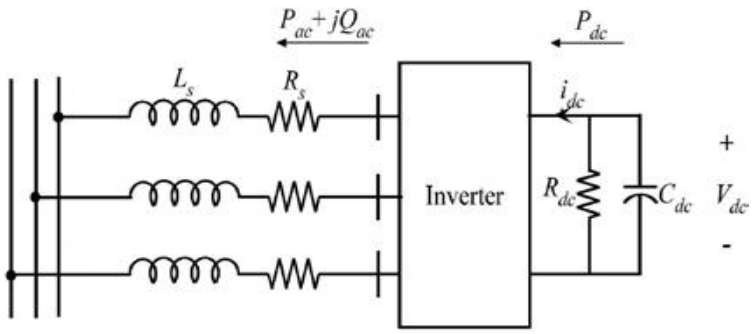

Figure 1. Equivalent circuit of STATCOM [26].

B. Active Power Line Conditioner (APLC)

Active power line conditioners (APLCs) can be considered as advanced shunt active power filters (APFs) that are strategically deployed at a limited number of selected buses. Unlike conventional APFs, which inject equal and opposite harmonic currents to completely eliminate distortions caused by nonlinear loads, APLCs are designed to generate optimized reference currents. These currents are determined to regulate both overall network and individual bus voltage total harmonic distortion (THDv) within acceptable limits as specified by power quality standards.

Existing research on APLCs has primarily concentrated on determining their optimal placement and sizing, along with analyzing their steady-state performance and control strategies. In most studies, APLCs are modeled as harmonic current sources that inject specific harmonic components at predetermined frequencies [13–18].

C. Proposed CPD with STATCOM and APLC Functions

Most existing studies focus on addressing either reactive power compensation or harmonic distortion mitigation independently. In contrast, the proposed custom power device (CPD) extends the functionality of a conventional APLC by incorporating reactive power support capability similar to that of a STATCOM.

This integrated configuration enables simultaneous management of reactive power and enhancement of voltage quality across individual buses as well as the entire network. The CPD achieves this by injecting optimally controlled active and reactive current components at both fundamental and harmonic frequencies.

The schematic representation of the proposed system is illustrated in Fig. 2, where detailed nonlinear models are employed for both the CPD controller and the inverter structure [27].

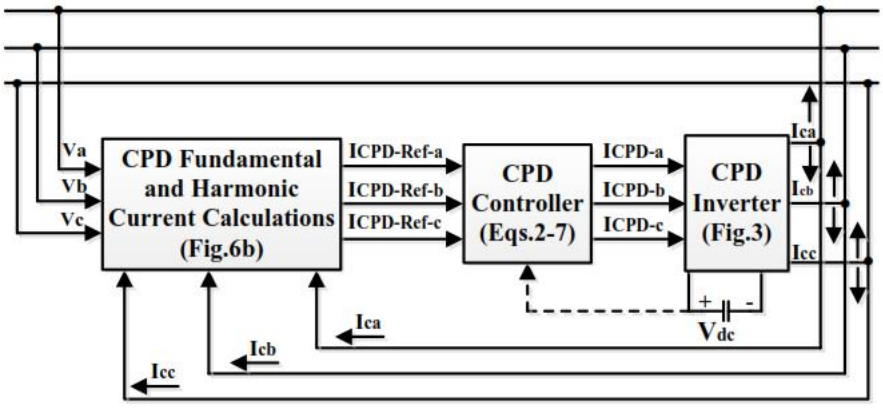

Figure 2: Schematic of the proposed CPD.

CPD Five-Level Neutral-Point Clamped Inverter

The inverter employed in the CPD is based on a five-level neutral-point clamped (FL-NPC) topology. The adopted three-phase inverter configuration, which feeds a series RL filter (comprising R_f and L_f) along with an AC back electromotive force (v), is illustrated in Fig. 3.

This multilevel structure is capable of generating five distinct output voltage levels, namely 0, $\pm\frac{V_{dc}}{4}$, and $\pm\frac{V_{dc}}{2}$, thereby enhancing voltage waveform quality and reducing harmonic distortion.

CPD Adaptive Hysteresis Current Control Design

An adaptive hysteresis current control (AHCC) strategy is employed for regulating the CPD inverter. It is assumed that the grounded neutral point of the system is directly connected to the midpoint of the five-level neutral-point clamped (FL-NPC) inverter. By applying Kirchhoff's Voltage Law (KVL) to phase-a of the system, the governing equation can be expressed as:

$$u_a = v_a + L_f \frac{di_{CPD,a}}{dt} + R_f i_{CPD,a} \qquad (2)$$

where v_a, $i_{\text{CPD},a}$, and u_a denote the phase-a voltage at the point of common coupling (PCC) on the AC side, the phase-a inverter (CPD) output current, and the phase-a inverter output voltage on the DC side, respectively.

To ensure a constant switching frequency, the fundamental component of the inverter output voltage is utilized for adjusting the hysteresis band, instead of relying directly on system parameters. When the phase-a leg of the FL-NPC inverter (Fig. 3) is assigned to inject the current i_a at the point of common coupling (PCC), the inverter must produce a voltage magnitude higher than the PCC voltage.

Ideally, the inverter generates a purely sinusoidal voltage waveform. However, due to the practical implementation of modulation techniques, the actual output voltage is non-sinusoidal. Consequently, the resulting current consists of two components: a fundamental component $i_{\text{CPD-F},a}$ and a switching ripple component $i_{\text{CPD-R},a}$, which can be expressed as:

$$i_{\text{CPD},a} = i_{\text{CPD-F},a} + i_{\text{CPD-R},a} \qquad (3)$$

Assuming that the voltage drops across the filter resistance R_f due to the ripple component is negligible compared to that across the filter inductance L_f, and substituting (3) into (2), the system dynamics can be simplified to:

$$\frac{di_{\text{CPD-R},a}}{dt} = \frac{u_a - L_f \frac{di_{\text{CPD-F},a}}{dt} + v_a}{L_f} = \frac{u_a - v_{a,\text{ideal}}}{L_f} \qquad (4)$$

where $v_{a,\text{ideal}}$ represents the fundamental component of the inverter output voltage for phase-a.

As illustrated in Fig. 4, four distinct operating regions (Areas 1–4) can be identified based on the magnitude of the ideal voltage. Correspondingly, different switching intervals are defined for each region.

$$\begin{cases} T_{1a} = \dfrac{V_{dc}}{4} \dfrac{1}{v_{ideal,a}} \left(\dfrac{2h_{a1}L_f}{\frac{V_{dc}}{4} - v_{ideal,a}} \right) \\ T_{2a} = \dfrac{V_{dc}}{4} \dfrac{2h_{a2}L_f}{\left(\frac{V_{dc}}{2} - v_{ideal,a}\right)\left(v_{ideal,a} - \frac{V_{dc}}{4}\right)} \\ T_{3a} = \dfrac{V_{dc}}{4} \dfrac{1}{\left(-v_{ideal,a}\right)} \left(\dfrac{2h_{a3}L_f}{\frac{V_{dc}}{4} + v_{ideal,a}} \right) \\ T_{4a} = \dfrac{V_{dc}}{4} \left(\dfrac{-2h_{a4}L_f}{\left(\frac{V_{dc}}{2} + v_{ideal,a}\right)\left(v_{ideal,a} + \frac{V_{dc}}{4}\right)} \right) \end{cases} \qquad (5)$$

Since the switching durations for Areas 1 and 3, as well as Areas 2 and 4, are identical, the conditions $T_1 = T_3 = 1/f_s$ and $T_2 = T_4$ are imposed to maintain a constant switching frequency. Using these conditions, the hysteresis band limits can be derived as functions of the DC-link voltage, filter inductance, switching frequency, and the ideal voltage component.

$$\begin{aligned} h_{a1} = h_{a3} = h_{a13} &= h_{\max}\left(\frac{|v_{ideal,a}|}{V_{dc}/4}\right)\left(1-\frac{|v_{ideal,a}|}{V_{dc}/4}\right) \\ h_{a2} = h_{a4} = h_{a24} &= h_{\max}\left(2-\frac{|v_{ideal,a}|}{V_{dc}/4}\right)\left(\frac{|v_{ideal,a}|}{V_{dc}/4}-1\right) \end{aligned} \qquad (6)$$

Here, $h_{\max} = \dfrac{V_{dc}}{8L_f f_{sw}}$

Selection of Hysteresis Band Shape

Based on the derived expressions, the hysteresis band profile depends on both the amplitude of the fundamental inverter voltage and the instantaneous value of the ideal reference voltage. Two distinct hysteresis band shapes are required to ensure proper AHCC operation under constant switching frequency conditions.

The selection between these two band shapes is governed by a threshold voltage level equal to $V_{dc}/4$. The difference between the ideal voltage and this threshold determines the transition points between the two hysteresis regions. Accordingly, the transition condition can be expressed as:

$$T_{\text{trans}} = |v_{\text{ideal},a}| - \frac{V_{dc}}{4} \qquad (7)$$

where T_{trans} denotes the transition instant between the two hysteresis band configurations.

Fig. 5 illustrates the resulting hysteresis band shapes derived from (6) and their switching mechanism based on (7). The overall hysteresis band h_a is constructed by alternating between the two band profiles, controlled through the transition signal. Specifically, when $T_{\text{trans}} < 0$, the control activates the hysteresis band h_{a13}; otherwise, the band h_{a24} is selected.

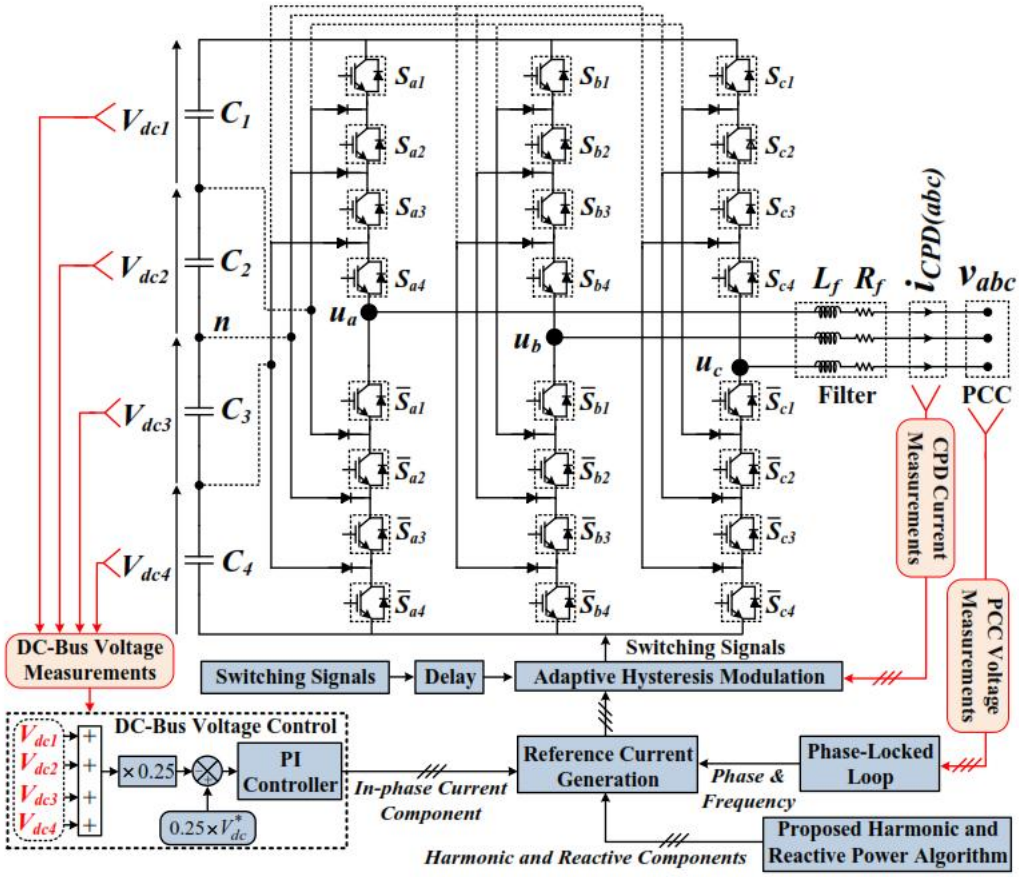

Figure 3: Detailed FL-NPC inverter structure of the proposed CPD.

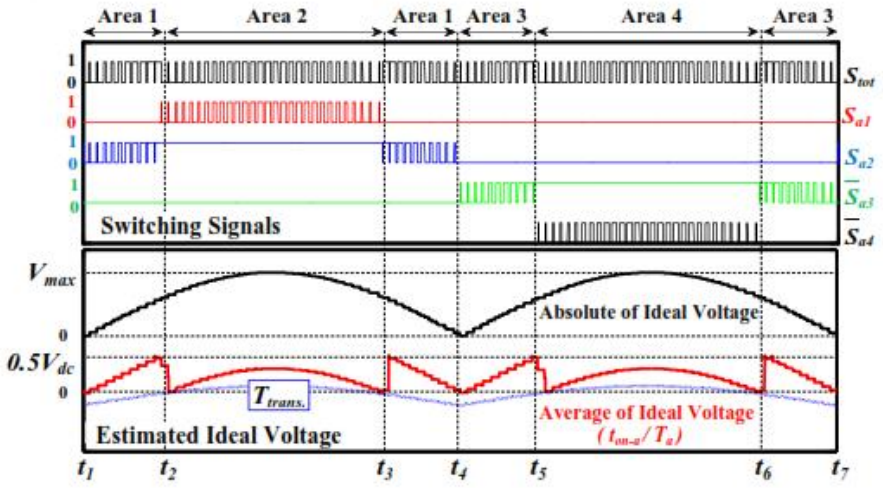

Figure 4: CPD generated FL-NPC inverter voltage using HCC with waveforms for Areas 1 to 4.

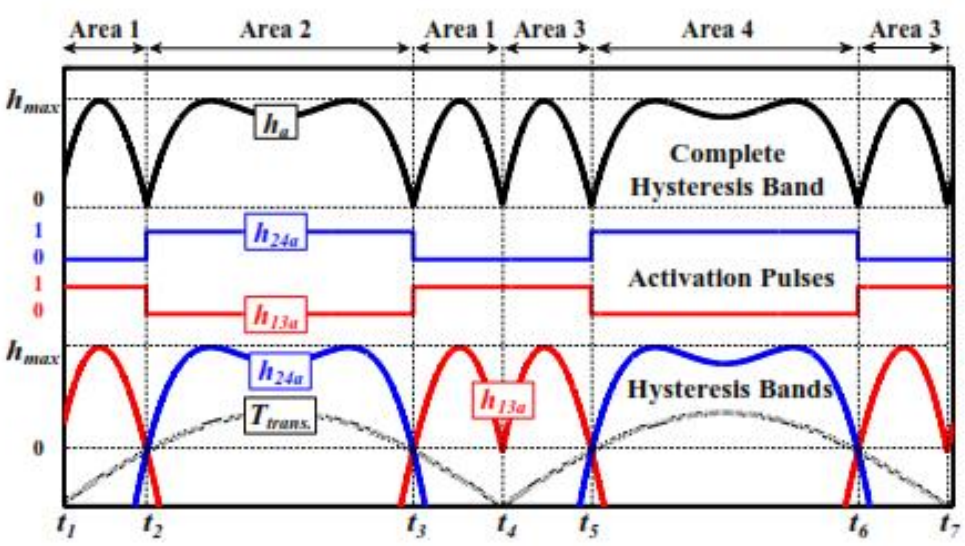

Figure 5: Hysteresis-shape selection according to Eqs. 6-7.

III. Problem Formulation for Optimal Siting and Sizing of Multiple CPDs

In this study, three-phase CPDs are modeled using five-level neutral-point clamped (FL-NPC) inverter configurations, as illustrated in Figs. 2–5. The nonlinear loads within the system are represented as harmonic current sources [9], injecting harmonic components at their respective connection points in the smart grid (SG).

This section presents the development of the first particle swarm optimization (PSO) algorithm aimed at determining the optimal placement (siting) and rating (sizing) of multiple CPDs within the network. The objective is to identify the most effective locations and corresponding capacities of CPDs to enhance overall system performance.

Accordingly, the rating of a CPD installed at bus $k$can be expressed as follows [13–18]:

$$I_{k,\text{CPD size}} = \sqrt{\sum_{h=1}^{H} |I_{k,\text{CPD}}^{(h)}|^2}, k = 1,2, \ldots, K \qquad (8)$$

where k and h denote the bus index and harmonic order (including the fundamental component), respectively, while $K$and Hrepresent their corresponding maximum values. The term $I_{k,\text{CPD}}^{(h)}$refers to the h^{th}harmonic current injected by the CPD installed at bus k.

The objective of the optimal siting and sizing problem is to minimize both the overall network voltage total harmonic distortion (THDv) and the aggregate size of the CPDs, which is characterized by their injected current magnitudes at fundamental and harmonic frequencies.

$$\min F_1 = W_{size} I_{CPDsizes} + W_{THD} THD_{v,network}$$
$$= W_{size} \sum_{k=1}^{K} I_{k,CPDsize} + W_{THD} \sum_{k=1}^{K} \sqrt{\sum_{h=2}^{H} \left|V_k^h\right|^2} / \left|V_{fund}\right|$$

Here, W_{size} and W_{THD} denote the weighting factors corresponding to CPD size and network THDv, respectively, while V_{fund} and V_k^h represent the fundamental and harmonic voltages at bus k.

The constraints associated with Eq. (9) include the upper $(V_{fund,max})$ and lower $(V_{fund,min})$ limits of the fundamental bus voltages [28], the upper limit of THDv $(THD_{V,max})$, and the maximum permissible limit for individual bus voltage harmonics $(V_{h,max})$ in accordance with IEEE-519 [10]. Additionally, an upper limit is imposed on the maximum size of each CPD, denoted as $I_{CPDsize,max}$.:

$$V_{fund,max} \geq V_{fund,k} \geq V_{fund,min} \quad (10)$$

$$THD_{v,k} = \sqrt{\sum_{h=2}^{H} \left(\frac{|V_k^h|}{|V_{fund}|}\right)^2} \leq THD_{v,max} \quad (11)$$

$$\frac{|V_k^h|}{|V_{fund}|} \leq V_{h,max} \quad (12)$$

$$I_{m,CPD} \leq I_{CPD\,size,max}, m = 1, \ldots, M \in MC \quad (13)$$

where $V_{fund,k}$ denotes the fundamental voltage at bus k, M represents the bus index, and MC denotes the set of candidate buses for CPD placement as specified by the utility.

A Particle Swarm Optimization (PSO) algorithm is developed and implemented to solve Eqs. (9)–(13). The process begins with an initial swarm comprising a set of randomly generated particles, representing candidate solutions (i.e., random locations and sizes of CPDs). An iterative procedure is then employed, in which each particle moves toward its best-known position and the global best position within the swarm, thereby converging toward the optimal solution [29].

At each iteration, the fitness of each particle is evaluated using Eq. (9). The best objective value achieved by an individual particle is referred to as *pbest*, while the best position among all particles in the swarm is denoted as *gbest*. The velocity of each particle is updated based on its relative position with respect to *pbest* and *gbest* [29]:

$$V_j^{n+1} = \omega V_j^n + C_1 \phi_1 \left(pbest_j^n - X_j^n\right) + C_2 \phi_2 \left(gbest^n - X_j^n\right) \quad (14)$$

where V_j^n and X_j^n denote the velocity and position of particle j at iteration n, respectively. The parameter ω represents the inertia weight factor, φ_1 and φ_2 are random numbers uniformly distributed between 0 and 1, and C_1 and C_2 are the cognitive and social acceleration coefficients, respectively.

The first PSO-based algorithm for the optimal siting and sizing of CPDs is illustrated in the flowchart shown in Fig. 6(a). The procedure can be summarized as follows:

1. CPDs are initially and temporarily installed at all candidate buses selected by the utility, i.e., $n_{candidate} = 1$ to $N_{candidate} \in MC$. In this study, the set of candidate buses MC includes all buses except the swing bus.
2. PSO particles are defined to represent the fundamental and harmonic current magnitudes (and phase angles) of each CPD at every candidate bus. For instance, in solving the optimization problem of Eq. (9) for the 15-bus system shown in Fig. 7, a total of 168 decision variables (particles) are required. This corresponds to 14 candidate buses, 2 variables (magnitude and phase angle) per CPD, and 6 frequency components (fundamental, 5th, 7th, 11th, 13th, and 17th harmonics), i.e., $14 \times 2 \times 6 = 168$.
3. The PSO algorithm is executed based on Eqs. (9)–(13) to determine the optimal sizes of CPDs (I_{CPD}) at the candidate buses.
4. Only those CPDs whose sizes exceed a predefined minimum threshold $(I_{CPD\ size,min}=0.01\ pu)$ are retained.
5. Finally, the selected CPDs are installed at their optimal locations $(n_{CPD,opt})$ with their corresponding optimal sizes $(I_{CPD,opt})$, and the results are recorded (e.g., as presented in Table 4 for the 15-bus system in Figs. 7–8).

The first PSO algorithm is executed under the worst operating condition (i.e., maximum linear and nonlinear loading levels).

Inputs: The inputs to the first PSO algorithm include the fundamental voltage $V_{fund,k}$ and harmonic voltages V_k^h at each bus, the weighting factors for CPD size and network THDv $(W_{size} = 0.5, W_{THD} = 0.5)$, the upper $(V_{fund,max}=1.1\ pu)$ and lower $(V_{fund,min}=0.9\ pu)$ limits for the fundamental bus voltages, the upper limit for THDv $(THD_{v,max}=0.05\ pu)$, and the maximum allowable limit for individual bus voltage harmonics $(V_{h,max}=0.03\ pu)$. Additionally, the utility-defined maximum CPD size $(I_{CPD\ size,max}=0.152\ pu)$, the minimum CPD size threshold $(I_{CPD\ size,min}=0.01\ pu)$, and the set of

candidate buses for CPD placement ($n_{candidate} = 1$ to $N \in MC$)—typically all buses except the swing bus—are considered.

Outputs: The outputs of the first PSO algorithm are the optimal CPD locations $(n_{CPD,opt} \in MC)$ and the corresponding optimal CPD sizes $(I_{CPD,opt})$, selected from among the candidate buses while satisfying the constraints defined in Eq. (13).

IV. Optimal Online Operation of the Allocated CPDs

The problem formulation for the online control of the allocated CPDs is based on the availability of smart meter data transmitted from each bus to the Smart Grid Central Controller (SGCC). The flowchart of the second PSO algorithm (based on Eqs. (15)–(16) and (10)–(12)) is illustrated in Fig. 6(b). This algorithm is similar to the first PSO algorithm (Eqs. (9)–(13)), with the following differences:

1. CPDs are installed only at the optimal locations $(n_{CPD,opt})$ determined by the first PSO algorithm.
2. The network operating conditions and the optimization of the objective function are updated at discrete time intervals Δt. The objective function in this stage is the minimization of the network total harmonic distortion of voltage (THDv):

$$\min F_2(t) = \sum_{k=1}^{K} \sqrt{\sum_{h=2}^{H} \left(\frac{|V_k^h(t)|}{|V_{fund}(t)|} \right)^2}, t = \Delta t, 2\Delta t, \ldots \qquad (15)$$

3. Constraint:

$$I_{n,CPD}(t) \leq I_{n,CPD}^{optimal}, \text{for } n_{CPD}^{optimal} \in MC_{optimal} \qquad (16)$$

where $n_{CPD}^{optimal}$ and $I_{n,CPD}^{optimal}$ denote the optimal locations and ratings of the allocated CPDs as determined by the first PSO algorithm.

4. The inputs to the second PSO algorithm (Fig. 6(b)) are similar to those of the first PSO algorithm (Fig. 6(a), with the following exceptions:

   i) The fundamental and harmonic bus voltages $(V_{fund,k}$ and $V_k^h)$ are obtained in real time via smart meters and updated at each time step Δt.

   ii) The maximum CPD sizes are set equal to the optimal ratings $(I_{CPD,opt})$ determined from the first PSO algorithm.

iii) The set of candidate buses is restricted to the optimal locations $(MC_{optimal})$.

5. The outputs of the second PSO algorithm are the optimal reference currents $(I_{CPD}(t))$for the CPD inverters connected at buses $(n_{CPD,opt})$, for $n = 1$ to $N_{CPD,opt}$, at each time step Δt. These currents are determined such that the overall network THDv and the individual bus voltage harmonics remain within the limits specified by IEEE-519 [10].

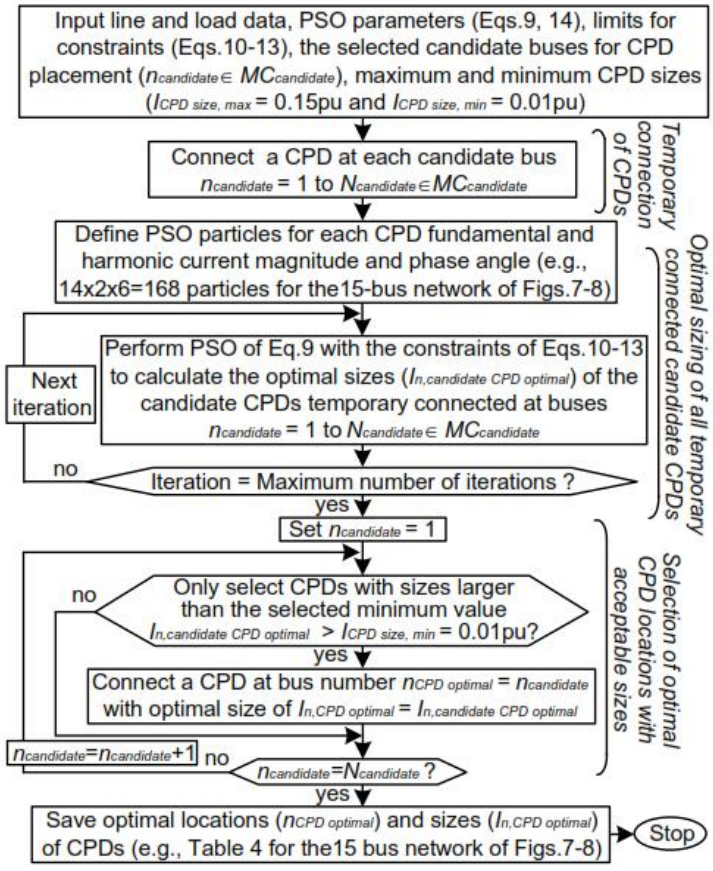

Figure 6: Flowcharts of the first PSO algorithm for optimal siting and sizing of CPDs based on Eqs.9-13

The second PSO algorithm begins by connecting the CPDs identified by the first PSO algorithm (Fig. 6) at their optimal locations $(n_{CPD,opt})$with their corresponding optimal sizes $(I_{CPD,opt})$. At each time step Δt, the following main steps are executed, as illustrated in Fig. 7.

Step 1: Real-time data transmitted from smart meters to the Smart Grid Central Controller (SGCC) are used to update the network state, including fundamental and harmonic bus voltages, as well as linear and nonlinear load conditions.

Step 2: PSO particles are defined to represent the fundamental and harmonic current magnitudes (and phase angles) of each CPD at the selected buses. For example, for the 15-bus system shown in Figs. 8–9, assuming that 3 CPDs are allocated by the first PSO algorithm, a total of 36 decision variables is required. This corresponds to 3 CPDs, 2 variables per CPD, and 6 frequency components (fundamental, 5th, 7th, 11th, and 13th harmonics), i.e., $3 \times 2 \times 6 = 36$.

Step 3: The PSO optimization problem defined in Eq. (15), subject to the constraints in Eqs. (10)–(12) and (16), is solved to determine the optimal reference currents $(I_{CPD}(t))$for the CPDs.

Step 4: The computed reference currents $(I_{CPD}(t))$are applied to control the CPD inverters, as described in Section II-C (Figs. 2–5 and Eqs. (2)–(7)).

Finally, the obtained solutions and corresponding waveforms are recorded (e.g., Table 8 and Fig. 10 for the 15-bus system shown in Figs. 8–9).

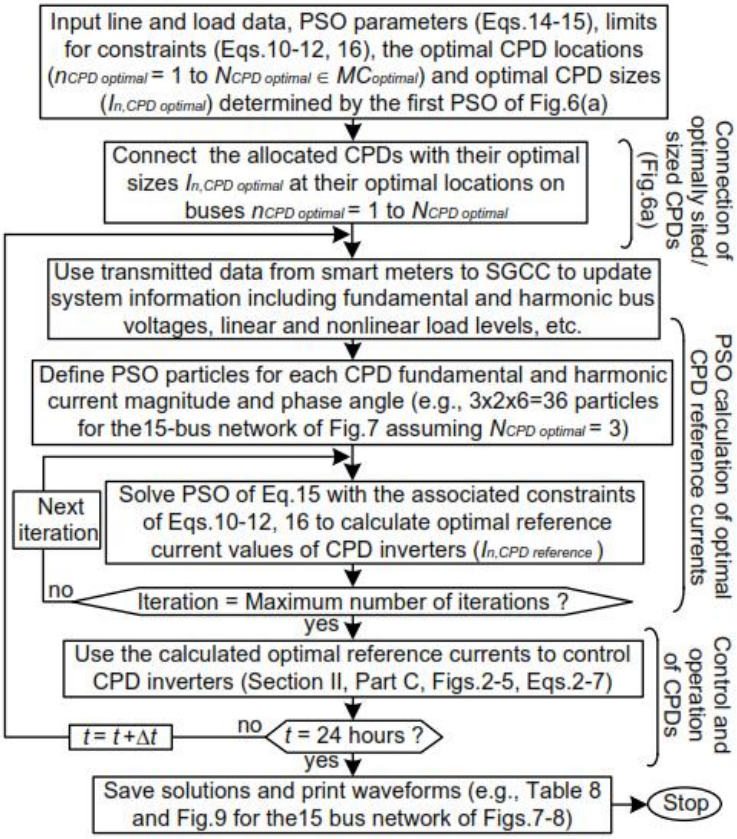

Figure 7: Flowcharts of the second PSO algorithm for optimal online control and operation of CPDs based on Eqs.15-16 and 10-12.

V. Simulations for Optimal Siting/Sizing and Real-Time Control of CPDs

The 15-bus, 60 Hz radial distribution network shown in Fig. 8 [25] is utilized to evaluate the performance of the proposed approaches for optimal siting and sizing (Fig. 6) and real-time control (Fig. 7) of multiple CPDs. The system includes six nonlinear loads located at buses 5, 7, 8, 10, 13, and 15.

The network line and linear load parameters are adopted from [25]. The selected base values are 2.5 MVA for power and 11 kV for voltage. Nonlinear loads are modeled using the conventional approach of harmonic current sources [9]. Table 1 summarizes the parameters of the nonlinear loads, which are represented as three-phase diode rectifiers supplying a resistive load of 6 Ω. The harmonic magnitudes and phase angles are derived to match the current distortions obtained from an accurate nonlinear model implemented in MATLAB/Simulink under rated sinusoidal terminal voltage conditions.

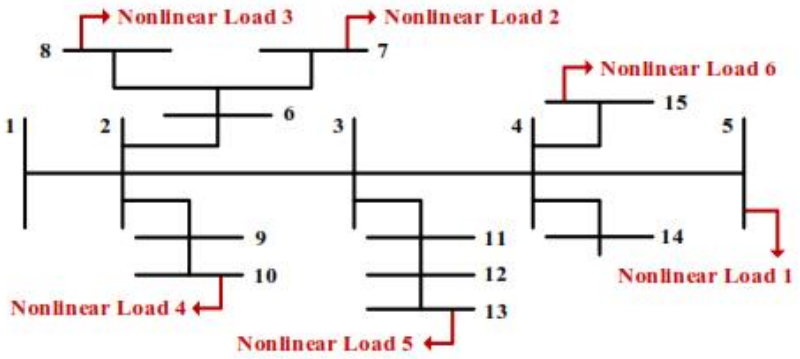

Figure 8. Single-line diagram of the 15-bus distorted SG [25] with 6 nonlinear loads (Table 1).

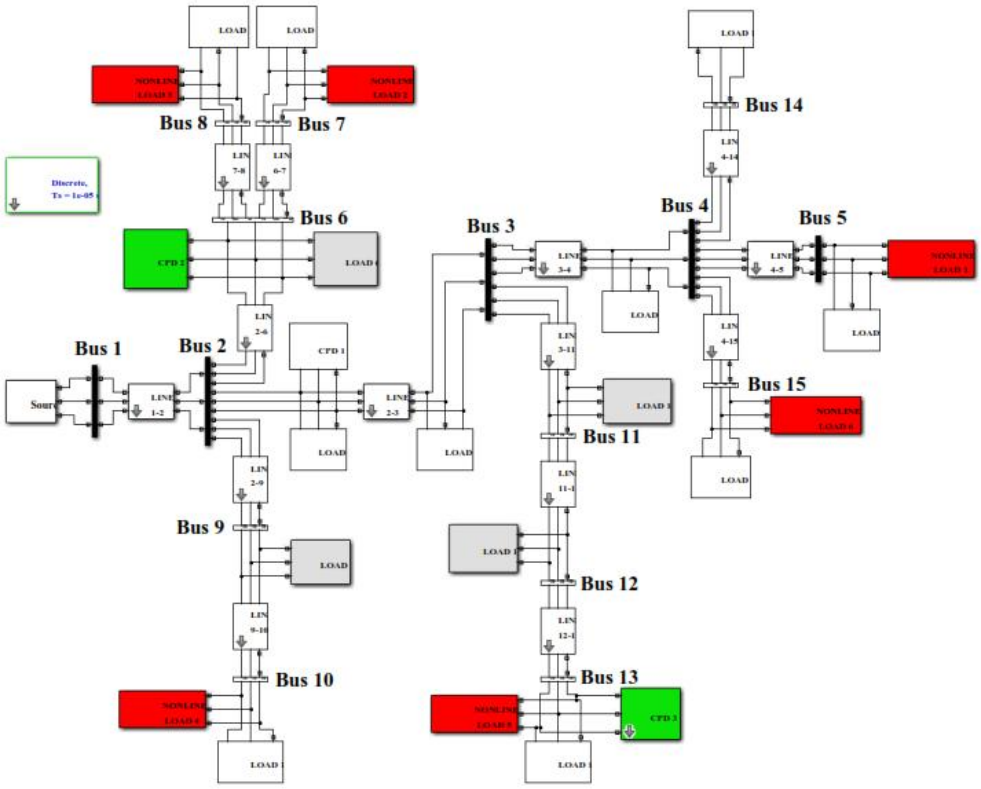

Figure 9: 15-bus distorted SG network modeled in Matlab/Simulink with 6 nonlinear loads and the three allocated optimal CPDs installed at buses 3, 6 and 13.

Table 1: Nonlinear load parameters for the network of Fig.8.

Harmonic Order	**5**	**7**	**11**	**13**	**17**
Harmonic Magnitude [%]*	22.60	11.34	9.02	6.49	5.63
Harmonic Phase Angle [degree]	180	180	0	0	180

* In percentage of the fundamental component.

Case 1: System Operation without CPDs

This case represents the worst operating condition of the system shown in Fig. 7, where all nonlinear loads are simultaneously activated. The simulation results are summarized in Table 2, which includes individual voltage harmonics (columns 2–6), THDv (column 7), and fundamental voltage magnitudes (V_{fund})(column 8) for all buses.

It is evident that the network experiences severe distortion. The harmonic voltages and THDv at all buses, as well as the fundamental voltages at most buses, violate the acceptable limits of 5% and 3%, respectively, while V_{fund}at several buses falls below the minimum permissible limit of 0.9 pu [28].

Bus 13 is identified as the most critically distorted location due to its remote position relative to the swing bus (bus 1), exhibiting a THDv of 20.99% and a fundamental voltage magnitude of 0.84 pu.

Table 2: Case 1- Network operation without any CPDs.

Bus	5	7	11	13	17	THDv [%]	V_{fund} [pu]
2	5.35	3.70	4.50	3.77	4.13	9.69	0.925
3	7.94	5.48	6.66	5.58	6.11	14.34	0.891
4	9.23	6.38	7.75	6.49	7.10	16.69	0.877
5	10.07	6.95	8.44	7.07	7.74	18.19	0.869
6	8.13	5.60	6.80	5.70	6.26	14.67	0.883
7	8.72	6.00	7.30	6.11	6.71	15.74	0.875
8	8.88	6.12	7.43	6.23	6.84	16.03	0.873
9	6.40	4.42	5.37	4.50	4.94	11.58	0.911
10	7.31	5.04	6.13	5.14	5.64	13.21	0.901
11	8.96	6.18	7.50	6.28	6.87	16.17	0.874
12	10.42	7.17	8.71	7.29	7.97	18.77	0.854
13	11.66	8.02	9.73	8.15	8.91	20.99	0.842
14	9.23	6.38	7.75	6.49	7.10	16.69	0.875
15	9.96	6.88	8.35	7.00	7.66	18.00	0.868
Ave.	**8.73**	**6.02**	**7.32**	**6.13**	**6.71**	**15.77**	**0.880**

Case 2: Optimal Siting and Sizing of Multiple CPDs

The first PSO algorithm (Fig. 6) is applied to determine the optimal locations and sizes of CPDs required to improve the voltage quality across the network (Fig. 7). The simulation results are presented in Table 3.

The optimal solution indicates the placement of three CPDs at buses 3, 6, and 13, with sizes of 0.152 pu, 0.120 pu, and 0.121 pu, respectively. Table 4 also provides the fundamental and harmonic compensation components of each CPD.

It is observed that the CPDs at buses 3 and 13 primarily compensate at the fundamental frequency, thereby contributing mainly to voltage regulation. In contrast, the CPD at bus 6 provides a balanced contribution to both voltage regulation and harmonic mitigation.

Compared to Case 1, the deployment of optimally sized and located CPDs ensures that all bus voltage harmonics, THDv values, and fundamental voltages are maintained within the permissible limits.

Table 3: Case 2 (CPD with both STATCOM and APLC Functions): Optimal siting and sizing of multiple CPDs for fundamental and harmonic compensations.

Bus	**5**	**7**	**11**	**13**	**17**	**THDv [%]**	**Vfund [pu]**	**ICPD [pu]**	**IStatCom [pu]**	**IAPLC [pu]**
2	0.71	0.64	0.69	0.04	0.07	2.23	0.945	0	0	0
3	0.69	0.26	0.49	0.44	0.20	3.04	0.923	0.152	0.119	0.093
4	1.87	1.07	1.49	0.44	0.78	3.88	0.909	0	0	0
5	2.61	1.58	2.12	0.97	1.38	4.91	0.900	0	0	0
6	0.53	1.34	0.97	0.21	0.43	4.57	0.910	0.120	0.078	0.090
7	1.06	1.71	1.41	0.18	0.03	4.87	0.902	0	0	0
8	1.20	1.81	1.54	0.28	0.12	4.98	0.900	0	0	0
9	1.68	1.32	1.52	0.71	0.86	3.42	0.930	0	0	0
10	2.52	1.89	2.23	1.30	1.54	4.75	0.920	0	0	0
11	0.71	0.18	0.17	1.09	0.73	3.03	0.913	0	0	0
12	0.74	0.10	0.56	1.99	1.46	3.75	0.905	0	0	0
13	0.76	0.13	1.03	2.74	2.07	4.99	0.902	0.121	0.107	0.055
14	1.87	1.07	1.49	0.44	0.78	3.87	0.907	0	0	0
15	2.52	1.51	2.04	0.90	1.30	4.76	0.900	0	0	0
Ave.	**1.39**	**1.04**	**1.27**	**0.84**	**0.84**	**4.07**	**0.912**	**-**	**-**	**-**
Total	**-**	**-**	**-**	**-**	**-**	**-**	**-**	**0.393**	**0.304**	**0.238**

Case 3: Optimal Siting and Sizing of CPDs Considering Only STATCOM Operation (Case 3)

In this case, the analysis of Case 2 is repeated with the first PSO algorithm executed considering only the fundamental frequency. Consequently, the CPDs operate as conventional STATCOM units, performing solely voltage regulation without accounting for harmonic distortions. The corresponding simulation results are presented in Table 5.

Compared to the results of Table 3, it is observed that the location of one CPD has changed, while the total installed CPD capacity is reduced by 27.13%. As expected, although all fundamental bus voltages are successfully regulated above the minimum acceptable limit of 0.9 pu, the voltage harmonic magnitudes and THDv values at all buses (except the swing bus) exceed the permissible limits.

Case 4: Optimal Siting and Sizing of CPDs Considering Only APLC Operation

This case is designed to demonstrate the capability of the proposed CPDs in improving the voltage quality of the entire network when operating as conventional Active Power Line Conditioner (APLC) units. In this scenario, the first PSO algorithm is executed considering only harmonic compensation. The simulation results are presented in Table 6.

Compared to the results of Table 3, it is observed that the locations of the three CPDs remain unchanged; however, their total installed capacity is significantly reduced by 40.6%. All bus voltage harmonic magnitudes and THDv values are maintained within the permissible limits. Nevertheless, most of the fundamental bus voltages are not adequately regulated, indicating the limitation of APLC-only operation in voltage support.

Case 5: Impacts of Weighting Factors

Table 4 presents an analysis of the significant impact of the objective function weighting factors (Eq. (9)) on the CPD siting and sizing solutions. As expected, larger values of W_{size} (e.g., 0.8 and 1.0) lead to solutions with more CPD units but smaller individual sizes, while the resulting network THDv approaches its maximum permissible limit of 5%.

Conversely, higher values of W_{THD} result in lower THDv levels. However, this improvement is achieved at the expense of installing a larger number of CPDs, similar to the conventional approach of placing active power filters (APFs) at all nonlinear buses, which is generally impractical.

Therefore, equal weighting factors (W_{size}=W_{THD}=0.5) are adopted in this study to achieve a balanced trade-off between CPD size and harmonic mitigation.

It is worth noting that if CPD cost is explicitly considered, a higher value of W_{size} would be preferred, encouraging the PSO algorithm to minimize the total installed CPD capacity. For instance, increasing W_{size} from 0.8 to 1.0 reduces the total CPD size by approximately 6.1% (from 0.361 pu to 0.339 pu), as indicated in Table 4.

Table 4: Case 5- Impacts of weighting factors (Eq.9) on optimal CPD siting/sizing solutions without the maximum CPD size constraint (Eq.13).

WTHD	Wsize	THDNet	ICPD	min F	CPD 1	CPD 2	CPD 3	CPD 4	CPD 5	CPD 6
0.0	1.0	4.53	0.339	0.339	Bus 5 / 0.043	Bus 7 / 0.036	Bus 8 / 0.062	Bus 10 / 0.018	Bus 13 / 0.126	Bus 15 / 0.054
0.2	0.8	4.13	0.361	1.115	Bus 5 / 0.039	Bus 8 / 0.103	Bus 9 / 0.041	Bus 13 / 0.125	Bus 15 / 0.0507	-
0.4	0.6	3.76	0.367	1.724	Bus 4 / 0.114	Bus 8 / 0.103	Bus 9 / 0.031	Bus 13 / 0.121	-	-
0.5*	**0.5***	**3.14**	**0.379**	**1.760**	**Bus 3 / 0.162**	**Bus 6 / 0.101**	**Bus 13 / 0.116**	-	-	-

0.6	0.4	2.77	0.387	1.817	Bus 4 / 0.119	Bus 8 / 0.107	Bus 9 / 0.039	Bus 13 / 0.122	-	-
0.8	0.2	1.50	0.394	1.279	Bus 5 / 0.055	Bus 8 / 0.100	Bus 9 / 0.047	Bus 13 / 0.129	Bus 15 / 0.063	-
1.0	0.0	0.120	0.406	0.120	Bus 5 / 0.052	Bus 7 / 0.049	Bus 8 / 0.071	Bus 10 / 0.045	Bus 13 / 0.129	Bus 15 / 0.061

Case 6: Optimal Real-Time Operation of Allocated CPDs

For the optimal real-time operation of the smart grid (SG) shown in Fig. 7 with a minimum number of CPDs, the following procedure is adopted:

Step 1: The first PSO algorithm (Fig. 6(a)) is executed to determine the optimal number, locations, and sizes of the required CPDs. As obtained in Case 2 (Table 3, column 9), three CPDs with sizes of 0.152 pu, 0.120 pu, and 0.121 pu are installed at buses 3, 6, and 13, respectively.

Step 2: At each time step Δt, the Smart Grid Central Controller (SGCC) receives updated network data from smart meters, computes the optimal CPD reference currents by executing the second PSO algorithm (Fig. 7), and transmits these reference signals to the CPDs.

Step 3: Each CPD utilizes the received reference currents to control its inverter and inject the required fundamental and harmonic currents into the SG network.

Figure 8 illustrates the MATLAB/Simulink model of the 15-bus SG system (Fig. 8) with the three optimally allocated CPDs connected at buses 3, 6, and 13. Simulations are conducted for various scenarios involving different numbers of simultaneously activated nonlinear loads. The corresponding results are presented in Figs. 9–10.

For each sub-case (Cases 6a–6e), detailed results including THDv and fundamental voltage magnitudes (V_{fund}), both without and with CPD operation, are provided.

Table 5: Case 6- Real-time system operation with the optimal number of CPDs as determined in Case 2 with different penetrations of nonlinear loads.

Case	Condition	Parameter	2	3	4	5	6	7	8	9	10	11	12	13	14	15	Ave. / Total
6a	Without CPDs	THD [%]	9.69	14.34	16.69	18.19	14.67	15.74	16.03	11.58	13.21	16.17	18.77	20.99	16.69	18.00	15.77
		Vfund [pu]	0.925	0.891	0.877	0.869	0.883	0.875	0.873	0.911	0.901	0.874	0.854	0.842	0.875	0.868	0.880
	With CPDs	THD [%]	2.23	3.04	3.88	4.91	4.57	4.87	4.98	3.42	4.75	3.03	3.75	4.99	3.87	4.76	4.07
		Vfund [pu]	0.945	0.923	0.909	0.900	0.910	0.902	0.900	0.930	0.920	0.913	0.905	0.902	0.907	0.900	0.912
	Injected CPD		-	0.152	-	-	0.120	-	-	-	-	-	-	0.121	-	-	**0.393**

	currents [pu]																
6b	Without CPDs	THD [%]	8.02	11.03	13.32	14.78	12.93	13.98	14.27	9.88	11.49	11.02	11.01	11.01	13.32	14.59	12.19
		Vfund [pu]	0.932	0.904	0.890	0.881	0.889	0.882	0.880	0.918	0.908	0.896	0.890	0.889	0.888	0.881	0.895
	With CPDs	THD [%]	2.21	2.87	3.70	4.74	4.53	4.87	5.00	3.41	4.76	2.70	3.21	4.40	3.69	4.59	3.91
		Vfund [pu]	0.945	0.924	0.909	0.900	0.910	0.902	0.900	0.931	0.920	0.915	0.909	0.908	0.907	0.900	0.913
	Injected CPD currents [pu]		-	0.152	-	-	0.113	-	-	-	-	-	-	0.017	-	-	**0.282**
6c	Without CPDs	THD [%]	6.53	9.61	10.79	10.79	9.02	9.02	10.29	8.36	9.94	11.36	13.84	15.97	10.79	12.02	10.60
		Vfund [pu]	0.939	0.910	0.900	0.899	0.909	0.907	0.899	0.924	0.914	0.892	0.872	0.860	0.898	0.891	0.901
	With CPDs	THD [%]	2.07	2.84	3.23	3.23	4.12	4.10	4.92	3.55	5.00	2.83	3.44	4.61	3.22	4.04	3.66
		Vfund [pu]	0.945	0.923	0.912	0.911	0.915	0.913	0.905	0.931	0.921	0.912	0.903	0.900	0.910	0.903	0.915
	Injected CPD currents [pu]		-	0.040	-	-	0.030	-	-	-	-	-	-	0.124	-	-	**0.194**
6d	Without CPDs	THD [%]	4.57	7.45	8.49	9.87	6.76	7.74	6.76	4.57	4.57	9.16	11.59	13.68	8.49	8.49	8.01
		Vfund [pu]	0.947	0.919	0.909	0.900	0.918	0.910	0.916	0.944	0.943	0.901	0.881	0.868	0.907	0.907	0.912
	With CPDs	THD [%]	2.06	3.13	3.72	4.83	4.45	4.99	4.43	2.04	2.04	3.37	4.00	4.97	3.71	3.71	3.68
		Vfund [pu]	0.952	0.929	0.919	0.910	0.924	0.916	0.921	0.949	0.948	0.917	0.905	0.900	0.917	0.917	0.923
	Injected CPD currents [pu]		-	0.034	-	-	0.025	-	-	-	-	-	-	0.089	-	-	**0.148**
6e	Without CPDs	THD [%]	3.20	4.72	5.86	5.86	3.20	3.20	3.20	4.98	6.52	4.72	4.71	4.71	5.86	7.04	4.84
		Vfund [pu]	0.953	0.931	0.920	0.919	0.938	0.936	0.935	0.939	0.928	0.923	0.916	0.915	0.918	0.911	0.927
	With CPDs	THD [%]	2.14	3.08	3.61	3.61	3.89	3.86	3.86	3.58	5.00	2.90	2.93	3.61	3.60	4.48	3.58
		Vfund [pu]	0.953	0.931	0.920	0.919	0.938	0.936	0.935	0.939	0.928	0.923	0.916	0.915	0.918	0.911	0.927
	Injected CPD currents [pu]		-	0.046	-	-	0	-	-	-	-	-	-	0	-	-	**0.046**

It should be noted that, unlike conventional Active Power Filters (APFs), which aim to completely eliminate harmonic distortions at the point of common coupling (PCC), the objective of the proposed CPDs is to regulate both bus-level and network-level THDv within the permissible limits.

Consequently, the post-compensation voltage waveform at bus 13 is not purely sinusoidal. However, a significant improvement in power quality is achieved, with the THDv reduced from 20.99% to 4.99%.

Analyses of the waveforms presented in Figs. 10(a)–10(d) reveal the following observations:

• The transient network conditions are primarily caused by switching events and variations in the number of active nonlinear loads.

• As shown in Fig. 10(a), the three CPDs effectively reduce the THDv of all buses to below 5% after a short transient period required for the CPD inverters to generate and inject the necessary compensation currents. It is also observed that the location of the most distorted bus varies depending on the number and locations of the activated nonlinear loads and may differ between transient and steady-state conditions.

• Figures 10(b) and 10(c) illustrate the magnitudes and waveforms of the three-phase CPD currents at bus 13. According to Table 5, the CPD current magnitudes at bus 13 are 0.089 pu, 0.124 pu, 0.017 pu, and 0.121 pu for Cases 6d, 6c, 6b, and 6a, respectively. At $t = 0.06$s (Case 6b), the nonlinear load at bus 13 is disconnected; consequently, as confirmed by Table 5 (row 14, column 13) and Figs. 10(b)–10(c), the injected CPD current at this bus is significantly reduced.

• In the absence of CPD operation (i.e., $t > 0.12$s), the fundamental voltage magnitudes (V_{fund}) at most buses fall below the recommended limit of 0.9 pu. In contrast, with CPDs in operation, all bus voltages are effectively regulated within the acceptable limits, as illustrated in Fig. 10(d).

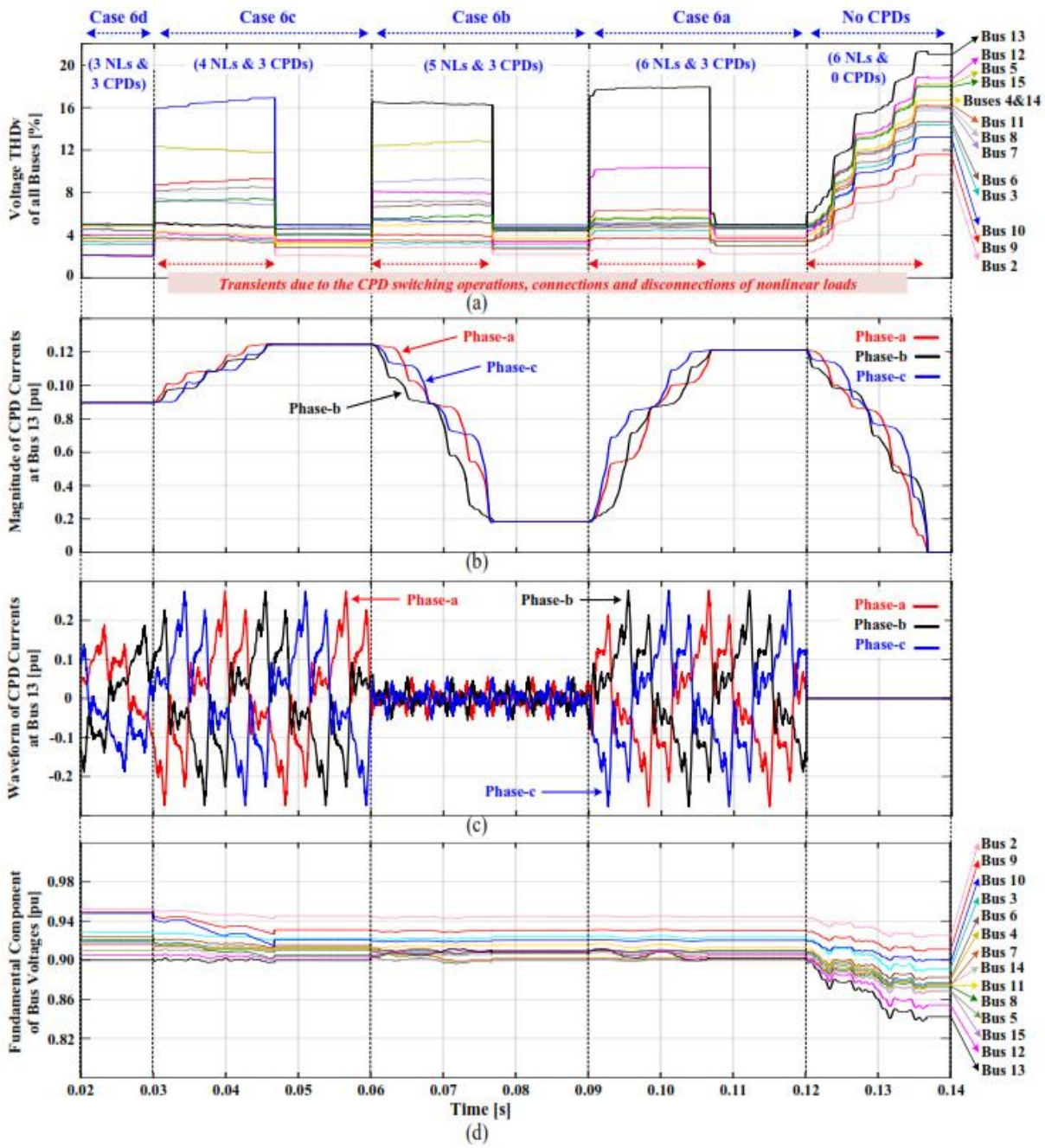

Figure 10: Optimal online operation of the 15-bus network for Cases 6d, 6c, 6b and 6a (Table 5) with three CPDs installed at optimal locations on buses 3, 6 and 13 with optimal ratings of 0.152pu, 0.120pu and 0.121pu, respectively; (a) THDv of all buses, (b) magnitudes of CPD injected currents at the worst node (bus 13), (c) CPD injected currents waveform at bus 13, (d) *Vfund* of all buses.

VI. CONCLUSIONS

The main conclusions drawn from the detailed simulations of the 15-bus distorted smart grid (SG) with six nonlinear loads (Figs. 7–8) are summarized as follows:

• The application of multiple CPDs, incorporating both STATCOM and APLC functionalities, effectively maintains the THDv of all buses within the permissible limit of 5%, while simultaneously regulating the fundamental bus voltages above the minimum acceptable limit of 0.9 pu (Tables 3–4, Fig. 10).

• The optimal number, sizes, and locations of CPDs depend on the SG configuration, constraint limits, and the number, types, and locations of nonlinear loads. The objective function weighting factors (Eq. (9)) significantly influence the siting and sizing results (Table 7). Larger values of W_{size}lead to solutions with more CPDs but smaller total capacity, with THDv values approaching the upper limit of 5%. In contrast, higher values of W_{THD} yield lower THDv levels but require a larger number of CPDs, increasing installation and maintenance costs. Therefore, equal weighting factors (W_{size}=W_{THD}=0.5) are recommended to achieve a balanced trade-off.

• The optimally allocated CPDs significantly enhance SG performance by enabling real-time control of network THDv and fundamental bus voltages (V_{fund})under varying operating conditions (Table 8, Figs. 9–10).

• The allocated CPDs can also be operated in a coordinated manner to function as either STATCOMs or APLCs in real time, enabling control of reactive power (and hence voltage regulation) at the fundamental frequency or mitigation of harmonic distortions across the network, as demonstrated in Tables 5 and 6, respectively.

VII. References

[1] F. Rahimi and A. Ipakchi, “Demand response as a market resource under the smart grid paradigm,” *IEEE Transactions on Smart Grid*, vol. 1, no. 1, pp. 82–88, 2010.

[2] B. D. Russell and C. L. Benner, “Intelligent systems for improved reliability and failure diagnosis in distribution systems,” *IEEE Transactions on Smart Grid*, vol. 1, no. 1, pp. 48–56, 2010.

[3] K. Moslehi and R. Kumar, “A reliability perspective of the smart grid,” *IEEE Transactions on Smart Grid*, vol. 1, no. 1, pp. 57–64, 2010.

[4] C. A. Cañizares and F. L. Alvarado, “Point of collapse and continuation methods for large AC/DC systems,” *IEEE Transactions on Power Systems*, pp. 1–8, 1993.

[5] R. C. Dugan, M. F. McGranaghan, and H. W. Beaty, *Electrical Power Systems Quality*. New York, NY, USA: McGraw-Hill, 1996.

[6] O. Anaya-Lara and E. Acha, "Modeling and analysis of custom power systems by PSCAD/EMTDC," *IEEE Transactions on Power Delivery*, vol. 17, no. 1, pp. 266–272, 2002.

[7] N. G. Hingorani and L. Gyugyi, *Understanding FACTS: Concepts and Technology of Flexible AC Transmission Systems*. New York, NY, USA: IEEE Press, 2000.

[8] P. H. Mohammadi and M. T. Bina, "A transformerless medium-voltage STATCOM topology based on extended modular multilevel converters," *IEEE Transactions on Power Electronics*, vol. 26, no. 5, pp. 1534–1545, 2011.

[9] E. F. Fuchs and M. A. S. Masoum, *Power Quality in Electrical Machines and Power Systems*, 2nd ed. USA: Academic Press (Elsevier), 2015.

[10] *IEEE Recommended Practices and Requirements for Harmonic Control in Electrical Power Systems*, IEEE Std 519-1992, 1993.

[11] B. Singh, K. Al-Haddad, and A. Chandra, "A review of active filters for power quality improvement," *IEEE Transactions on Industrial Electronics*, vol. 46, no. 5, pp. 960–971, 1999.

[12] D. D. Sabin and A. Sannino, "A summary of the draft IEEE P1409 custom power application guide," *IEEE PES Transmission and Distribution Conference and Exposition*, vol. 3, pp. 931–936, 2003. [Online]. Available: http://grouper.ieee.org/groups/1409/0309_sannino.pdf

[13] Y. Y. Hong and Y. K. Chang, "Determination of locations and sizes for active power line conditioners to reduce harmonics in power systems," *IEEE Transactions on Power Delivery*, vol. 11, no. 3, pp. 1610–1617, 1996.

[14] W. K. Chang and W. M. Grady, "Minimizing harmonic voltage distortion with multiple current-constrained active power line conditioners," *IEEE Transactions on Power Delivery*, vol. 12, no. 2, pp. 837–843, 1997.

[15] I. Ziari and A. Jalilian, "A new approach for allocation and sizing of multiple active power-line conditioners," *IEEE Transactions on Power Delivery*, vol. 25, no. 2, pp. 1026–1035, 2010.

[16] K. Kennedy, G. Lightbody, R. Yacamini, M. Murray, and J. Kennedy, "Online control of an APLC for network-wide harmonic reduction," *IEEE Transactions on Power Delivery*, vol. 21, no. 1, pp. 432–439, 2006.

[17] K. Kennedy, G. Lightbody, R. Yacamini, M. Murray, and J. Kennedy, "Development of a network-wide harmonic control scheme using an active filter," *IEEE Transactions on Power Delivery*, vol. 22, no. 3, pp. 1847–1856, 2007.

[18] H. A. Ramos-Carranza and A. Medina, "Single-harmonic active power line conditioner for harmonic distortion control in power networks," *IET Power Electronics*, vol. 7, no. 9, pp. 2218–2226, 2014.

[19] B. Singh, K. Al-Haddad, and A. Chandra, "A universal active power filter for single-phase reactive power and harmonic compensation," in *Proc. Power Quality Conf. (Power Quality '98)*, Hyderabad, India, pp. 81–87, 1998.

[20] W. Oliveira and P. M. Santos, "Transformerless single-phase universal active power filter for harmonic and reactive power compensation," *IEEE Transactions on Power Electronics*, vol. 29, no. 7, pp. 3563–3572, 2014.

[21] T. B. Kumar and M. V. G. Rao, "Mitigation of harmonics and power quality enhancement for SEIG-based wind farm using ANFIS-based STATCOM," in *Proc. Int. Conf. Smart Electric Grid (ISEG)*, Guntur, India, pp. 1–7, 2014.

[22] B. B. Ambati and V. Khadkikar, "Optimal sizing of UPQC considering VA loading and maximum utilization of power electronic converters," *IEEE Transactions on Power Delivery*, vol. 29, no. 3, pp. 1490–1498, 2014.

[23] V. Khadkikar and A. Chandra, "UPQC-S: A novel concept of simultaneous voltage sag/swell and load reactive power compensation utilizing series inverter of UPQC," *IEEE Transactions on Power Electronics*, vol. 26, no. 9, pp. 2414–2425, 2011.

[24] S. Ganguly, "Multi-objective planning for reactive power compensation of radial distribution networks with unified power quality conditioner allocation using particle swarm optimization," *IEEE Transactions on Power Systems*, vol. 29, no. 4, pp. 1801–1810, 2014.

[25] D. Das, D. P. Kothari, and A. Kalam, "Simple and efficient method for load flow solution of radial distribution networks," *International Journal of Electrical Power & Energy Systems*, vol. 17, no. 5, pp. 335–346, 1995.

[26] M. Moghbel and M. A. S. Masoum, "D-STATCOM based on hysteresis current control to improve voltage profile of distribution systems with PV solar power," in *Proc. Australasian Universities Power Engineering Conf. (AUPEC)*, Brisbane, QLD, Australia, pp. 1–5, 2016.

[27] A. Fereidouni, *"Shunt Active Power Filter Enhancement Using Advanced Control and Modulation Techniques,"* Ph.D. dissertation, Curtin University, Perth, Australia, 2016.

[28] *Australian Standard Voltage Levels*, AS 60038-2012. [Online]. Available: http://infostore.saiglobal.com.au

[29] Y. del Valle, G. K. Venayagamoorthy, S. Mohagheghi, J. C. Hernandez, and R. G. Harley, "Particle swarm optimization: Basic concepts, variants and applications in power systems," *IEEE Transactions on Evolutionary Computation*, vol. 12, no. 2, pp. 171–195, 2008.